Materials Horizons

ROYAL SOCIETY OF CHEMISTRY

COMMUNICATION

View Article Online
View Journal

Cite this: DOI: 10.1039/d5mh00991j

Received 26th May 2025,
Accepted 21st July 2025

DOI: 10.1039/d5mh00991j

rsc.li/materials-horizons

High-performance organic thermoelectric materials based on n-type conjugated polymers *via* chemical isomerization-induced charge transport modulation†

Hojun Ji,‡[a] Jeong Gye Lee,‡[a] Hyunji Lee,[a] Daegun Kim *[b] and Kilwon Cho *[a]

High-performance n-type conjugated polymer-based thermoelectric (TE) materials remain scarce, despite their critical necessity in realizing wearable TE generators. Here, we sought to optimize TE charge transport in the n-type conjugated polymer poly(benzodifurandione) (PBFDO) *via* the incorporation of the isomeric monomer, benzodipyrandione (BPDO). BFDO segments in the PBFDO chain were systematically converted to BPDO segments *via* chemical isomerization driven by hydrothermal treatment. Hydrothermal treatment decreased the carrier density, whereas the conversion of BFDO to BPDO improved the chain planarity and crystalline structure, featuring favorable electrical conduction. Moreover, the presence of BPDO segments transformed the transport mode of low-energy charge carriers from fluctuation-induced tunneling (FIT) to nuclear tunneling (NT). This energy-filtering effect significantly enhanced the Seebeck coefficient to 48 μV K^{-1}, yielding an n-type conjugated polymer with both a high power of 142 μW m^{-1} K^{-2} and a high electrical conductivity of 640 S cm^{-1}.

New concepts

This study introduces a refined backbone modification strategy based on chemical isomerization to enhance charge transport in a newly developed n-type conjugated polymer, addressing the longstanding challenge of achieving high-performance n-type organic thermoelectric (TE) materials. By incorporating an isomeric monomer—benzodipyrandione (BPDO)—into the poly(benzodifurandione) (PBFDO) backbone *via* hydrothermal treatment, we enable molecular transformation from BFDO to BPDO segments. This structural rearrangement leads to improved backbone planarity and crystallinity, facilitating efficient charge carrier mobility. Crucially, the isomerization not only reduces carrier density but also modulates the dominant charge transport mechanism from fluctuation-induced tunneling to nuclear tunneling, inducing an energy-filtering effect that dramatically boosts the Seebeck coefficient. Through this, this work uniquely combines chemical isomerization with transport mode engineering, resulting in an n-type conjugated polymer with both high electrical conductivity (640 S cm^{-1}) and power factor (142 μW m^{-1} K^{-2}). Our findings open up promising directions and new avenues in conjugated polymer design by demonstrating how backbone isomerization can be strategically employed to achieve balanced and efficient TE properties in organic thermoelectric materials.

1. Introduction

Thermoelectric (TE) generation is a promising energy harvesting technology that harnesses waste heat produced during energy conversion processes.[1] TE generators can be applied to a wide range of systems including power plants, vehicles, electronics and wearable devices,[2–4] as well as applications in intelligent systems including thermoreceptors,[5] fire warning[6,7] and smart buildings.[8] In particular, TE generators have received great interest as a power source for wearable devices. Because biological homeostasis maintains the human body at a constant temperature, wearable TE generators can stably generate electricity. This stands in contrast to other energy harvesting technologies such as photovoltaics, piezoelectric generators, and triboelectric generators, all of which supply power intermittently according to their inherent mechanisms.[9] TE conversion is governed by the thermal diffusion of electrons or holes, and the TE figure-of-merit ZT value is defined as $S^2\sigma T/k$, where S is the Seebeck coefficient, σ is the electrical conductivity, T is the temperature, and k is the thermal conductivity.[10] Traditional TE materials were often based on heavy metals because of their high ZT values; however, the mechanical rigidity and toxicity of those metals have limited their use in wearable TE generators.[11] With the development of conducting polymers by the reduction (n-type) or oxidation (p-type) of conjugated systems, organic-based TE materials have attracted increasing attention on account of their advantages over traditional TE materials, which include mechanical flexibility, biocompatibility, low-cost processing and inherently low thermal conductivity.

Great advances have been made in organic-based TE materials in recent decades, with high ZT values of 0.42[12] (poly(3,4-ethylenedioxythiophene):polystyrene sulfonate, PEDOT:PSS),

[a] Department of Chemical Engineering, Pohang University of Science and Technology (POSTECH), Pohang 37673, Korea. E-mail: kwcho@postech.ac.kr
[b] School of Chemical, Biological and Battery Engineering, Gachon University, Seongnam 13120, Korea. E-mail: daegunkim@gachon.ac.kr

† Electronic supplementary information (ESI) available: Fig. S1–S10. See DOI: https://doi.org/10.1039/d5mh00991j

‡ These authors contributed equally.

0.25[13] (PDPPSe-12) and 0.40[14] (DPP-BTz) achieved at temperatures close to room temperature. New organic-based TE materials with ever higher *ZT* values have been developed, such that the *ZT* values of organic-based TE materials now rival those of traditional bulk TE materials at room temperature. However, these advances in TE performance have been primarily achieved in p-type conjugated polymers. Progress in n-type conjugated polymers has been comparatively limited, because the highly doped state is difficult to stabilize in n-type conjugated polymers.[15–17] The thermal conductivities of p-type and n-type conjugated polymers are both on the order of 0.1 W m^{-1} K^{-1}. However, the n-type conjugated polymers reported to date had low electrical conductivities, with an electrical conductivity >100 S cm^{-1} only achieved very recently.[18] By contrast, p-type conjugated polymers with electrical conductivities exceeding 1000 S cm^{-1} have been repeatedly reported.[19,20] Consequently, only a few n-type conjugated polymers have demonstrated a power factor ($S^2\sigma$) exceeding 100 μW m^{-1} K^{-2}. However, the low electrical conductivities of those polymers create problems,[21–23] as electrical conductivities below 500 S cm^{-1} can cause intense Joule heating during TE generation, limiting practical applications due to potential flattening of the temperature gradient across the TE material.

The low power factors of n-type conjugated polymers have been attributed to the absence of n-type dopants that stably induce the highly-doped state. n-type dopants such as 4-(2,3-dihydro-1,3-dimethyl-1*H*-benzimidazol-2-yl)-*N*,*N*-dimethylbenzenamine (N-DMBI) and tetrakis(dimethylamino)ethylene (TDAE) should have high reducing power for efficient doping, but their electron-rich characteristics are likely to cause oxidative degradation by ambient oxygen and water molecules.[24] Moreover, n-type conjugated polymers often contain a collection of aromatic rings to stabilize negative polarons upon doping.[25] Such chain backbones force the use of non-polar solvents, in which electron-rich n-type dopants are poorly soluble.[26–28] As a result, n-type conjugated polymers have shown poor doping efficiency and, as a result, low electrical conductivity.

Recently, Tang and coworkers reported a highly-doped n-type conjugated polymer based on poly(benzodifurandione) (PBFDO).[29] PBFDO was synthesized through oxidative polymerization and tetramethyl-*p*-benzoquinone (TMQ) was reduced to TMQH, which was oxidized back to TMQ upon reducing the PBFDO chain. Consequently, a highly-doped n-type $(PBFDO)^{m-}$:mH^+ system was realized, exhibiting an outstanding electrical conductivity of 2000 S cm^{-1}. Despite this high electrical conductivity, the power factor of PBFDO remained modest (90 μW m^{-1} K^{-2}) due to its small Seebeck coefficient. Interestingly, the repeat unit of PBFDO, benzodifurandione (BFDO), has a chemical isomer in which the pentagonal furanone is replaced with a hexagonal pyranone.[30,31] The chemical isomer of BFDO, benzodipyrandione (BPDO), forms a ladder structure upon polymerization and this structure was reported to be resistant to doping. Therefore, BFDO-to-BPDO isomerization was suppressed during PBFDO polymerization to extend the doping level in PBFDO. However, the effect of this suppression on TE charge transport has not been studied. The TE power factor includes both the Seebeck coefficient and the electrical conductivity, where the electrical conductivity depends on the overall carrier mobility and the Seebeck coefficient depends on the energy-dependent distribution of carrier mobility.[32] The introduction of BPDO segments into PBFDO could alter the energetic structure, which is not favorable for electrical conduction but could possibly promote TE charge transport. Thus, the suppression of BFDO-to-BPDO isomerization during PBFDO polymerization may have increased the electrical conductivity but decreased the power factor.

In this work, the TE power factor of PBFDO was successfully increased by introducing BPDO segments *via* hydrothermal treatment. The hydrothermal treatment of the PBFDO solution induced partial chemical isomerization, the extent of which was systematically modulated by the water content (γ). Changes in the chemical structure were identified through spectroscopic analyses such as nuclear magnetic resonance (NMR) spectroscopy, ultraviolet-visible-near infrared (UV-Vis-NIR) spectroscopy, and Raman spectroscopy. The conversion of BFDO to BPDO decreased the carrier density, but increased the carrier mobility as a result of improved chain planarity and crystalline structure. The presence of BPDO segments also transformed the transport mode, selectively inducing nuclear tunneling (NT) dominant transport for low-energy charge carriers while high-energy charge carriers maintained fast fluctuation-induced tunneling (FIT) transport. This energy-filtering effect significantly improved the Seebeck coefficient to 48 μV K^{-1}. As a result, a high power factor of 142 μW m^{-1} K^{-2} and a high electrical conductivity of 640 S cm^{-1} were simultaneously achieved, highlighting the potential of this polymer in practical applications.

2. Results and discussion

2.1. Structural transition from BFDO to BPDO

The BFDO unit has an isomer BPDO in which the pentagonal furanone ring of the bifurandione heterocyclic structure is replaced by a hexagonal pyranone ring. The polymerization of BPDO yields a conjugated ladder polymer, which has high planarity but poor doping efficiency. Therefore, in previous work on PBFDO, isomerization from BFDO to BPDO was suppressed in order to maximize the electrical conductivity. However, the highly planar BPDO structure could be beneficial for TE charge transport, as an increase in the carrier concentration would lower the transport energy level of conducting charge carriers, thus reducing the Seebeck coefficient.[33] Therefore, we explored the effect of isomerization in PBFDO on the TE properties of the polymer by inducing the fractional isomerization from BFDO to BPDO in PBFDO. The BFDO unit undergoes spontaneous isomerization under hot and humid conditions as a result of hydrolysis (Fig. 1a).[31] To induce isomerization in PBFDO, the water content γ of a PBFDO solution was varied, with each solution maintained at 120 °C for 12 h.

The changes in chemical structure induced by the hydrothermal treatment were investigated using nuclear magnetic resonance (NMR) spectroscopy. PBFDO exhibited a characteristic trident-shaped group of three peaks at chemical shifts (δ)

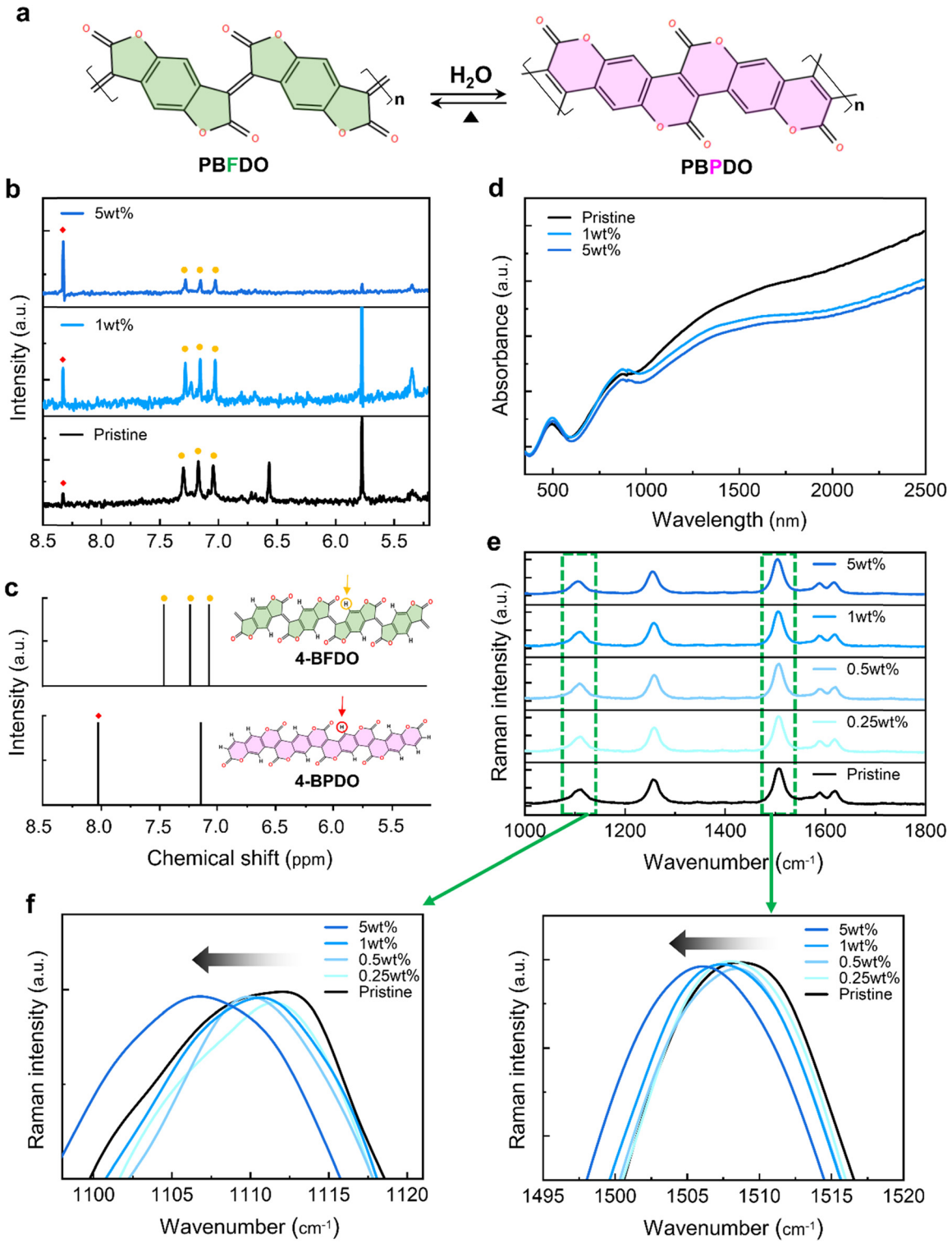

Fig. 1 (a) Chemical isomerization between PBFDO and PBPDO. (b) ^{1}H NMR spectra of PBFDO/BPDO samples with hydrothermal treatment of different γ values. (c) DFT-calculated ^{1}H NMR spectra of 4-BFDO and 4-BPDO. (d) UV-Vis-NIR absorption spectra, (e) Raman spectra and (f) Raman peaks that correspond to the aromatic C=C stretching of PBFDO/BPDO samples with respect to γ.

in the range of 7.0 to 7.5 ppm (Fig. 1b). These peaks were well identified in a DFT simulation of the 4-BFDO oligomer (Fig. 1c). Interestingly, a peak at δ = 8.3 ppm was also observed. This peak was featured in the DFT simulation of the 4-BPDO oligomer, indicating that PBFDO initially contained a small fraction of BPDO segments, possibly derived from natural isomerization or unintended insertion of BPDO during the synthesis of PBFDO. For the PBFDO solutions containing water

subjected to hydrothermal treatment, the intensity of the NMR peak corresponding to the BPDO segment increased markedly as γ increased from 1 to 5 wt%, indicating the fractional isomerization of BFDO to BPDO. This trend was also observed when the hydrothermal treatment temperature or treatment time was increased (Fig. S1, ESI†). The structural coherence of BPDO and BFDO units resulted in similar thermal stability (Fig. S2, ESI†) in the PBFDO/BPDO films compared to the pristine PBFDO film. The ratio of BFDO to BPDO, however, was difficult to accurately quantify due to the insufficient NMR resolution of the polymer specimen and the chemical similarity between BFDO and BPDO. Therefore, γ was used as an indicator of the extent of the transition to BPDO.

The changes in electronic structure that accompanied the structural changes induced by the hydrothermal treatment were explored using UV-Vis-NIR spectroscopy. The UV-Vis-NIR spectra of the pristine PBFDO film and films of PBFDO subjected to hydrothermal treatment with 1 and 5 wt% water showed trends typical of highly-doped conjugated polymers, with a relatively sharp peak at <900 nm and a broad absorption at >1200 nm (Fig. 1d).[29,34,35] Those peaks originated from the 0-0 transition in the neutral chain segment and the charged chain segment interacting with polarons and bipolarons, respectively.[36] The hydrothermal treatment reduced the relative absorption of polarons to the neutral peak, implying a reduction in carrier concentration compared to the pristine PBFDO film.[37] The reduction in carrier concentration upon hydrothermal treatment was also chemically identified by X-ray photoelectron spectroscopy (XPS) (Fig. S3, ESI†).

The relation between decrease in the carrier concentration and the change in chemical structure was examined using Raman spectroscopy (Fig. 1e). The pristine PBFDO film exhibited noticeable Raman peaks near 1100 and 1500 cm^{-1}, both of which can be assigned to stretching of the C_α═C_β bond.[38] Both of these peaks were red-shifted upon hydrothermal treatment, with the degree of red shift also increasing with increasing γ (Fig. 1f). This Raman shift is the opposite of what would be expected for the change in carrier concentration that occurs during typical dedoping processes, in which annihilation of polarons in the polymer backbone causes a transition from a quinoidal to benzoidal (or benzenoidal) form in the resonant state, inducing a blue shift of the Raman peaks. This phenomenon has been frequently observed in previous studies on doping of conjugated polymers.[39–41] PBFDO also showed a blue shift of the Raman peaks when the film was simply dedoped using a basic solvent (Fig. S4, ESI†). Specifically, the carrier concentration of PBFDO was reduced without causing structural changes by adding NaOH, which can passivate protons that balance the negative polarons in PBFDO chains, thus reducing the carrier concentration. The addition of NaOH blue-shifted the Raman peaks related to the C_α═C_β bond, indicating that polaron annihilation by NaOH treatment caused the transition from the quinoidal to benzenoidal form in the PBFDO chain. The observation of a red shift upon hydrothermal treatment, therefore, implies that the system underwent a chemical structural change that compensated for the transition to the benzenoidal form, improving the planarity of the polymer backbone. The conjugated ladder structure formed by BPDO segments has superior planarity compared with the BFDO-only system. The hydrothermal treatment-induced red shift of the absorption peak related to C═C stretching in the Fourier-transform infrared (FT-IR) spectra indicated that the BFDO-to-BPDO isomerization gave rise to improved delocalization of π electrons along the chain backbone (Fig. S5, ESI†).[42] In conjunction with the UV-Vis-NIR and FT-IR data, the Raman spectroscopic data supported the NMR results, suggesting the chemical isomerization of BFDO to BPDO.

2.2. Microstructures of PBFDO/BPDO films

The Raman spectroscopy results presented above indicated that the chemical isomerization was accompanied by changes in the chain backbone structure. Such a change in polymer backbone structure would affect the micro-scale crystalline structure, which in turn would influence the TE charge transport behavior.[43,44] Two-dimensional grazing incident wide angle X-ray scattering (2D GIWAXS) analysis of the pristine PBFDO film showed noticeable (h00) peaks in the out-of-plane direction and a (010) peak in the in-plane direction (Fig. 2a). The (h00) and (010) peaks correspond to the lamellar spacing and the π–π distance in PBFDO crystalline lamellae, respectively (Fig. 2b). The 2D GIWAXS results, therefore, indicate that the pristine PBFDO film is composed of a well-ordered edge-on configuration of crystallites. The PBFDO/BPDO films after hydrothermal treatment also showed good edge-on configurations for various γ values (Fig. S6, ESI†). However, the values of both the lamellar spacing and π–π distance varied depending on the water content used for hydrothermal treatment (Fig. 2c and d). The (100) peak shifted from 0.594 to 0.587 $Å^{-1}$ as γ was increased from 0 to 5 wt%, corresponding to an increase in lamellar spacing from 10.6 to 10.7 Å (Fig. 2e). In contrast, the (010) peak shifted from 1.82 to 1.83 $Å^{-1}$, corresponding to a decrease in π–π distance from 3.45 to 3.43 Å.

It is noteworthy that the lamellar spacings of the PBFDO films were far lower than those of conventional conjugated polymer crystallites. For example, the lamellar spacing in poly(3-hexylthiophene) (P3HT) lies in the range 16–18 Å and that of poly[2,5-bis(3-tetradecylthiophen-2-yl)thieno[3,2-*b*]thiophene] (PBTTT) lies in the range 20–22 Å.[45–47] The relatively small lamellar spacing of the PBFDO film can be attributed to the absence of side chains. Compared to other conjugated polymer films, the lamellar spacing of the PBFDO film would be expected to be more sensitive to the characteristics of the polymer backbone. In this context, the slight variation in lamellar spacing observed upon BFDO-to-BPDO isomerization is reasonable, as even minor changes in the backbone configuration can affect packing structure in the absence of bulky side chains. A decrease in the carrier concentration upon hydrothermal treatment implies that the counter cations that balanced the negative polarons were released from the polymer backbone. The removal of counter ions often decreases the lamellar spacing in highly-doped conjugated polymer films as the steric hindrance caused by the inserted counter ions

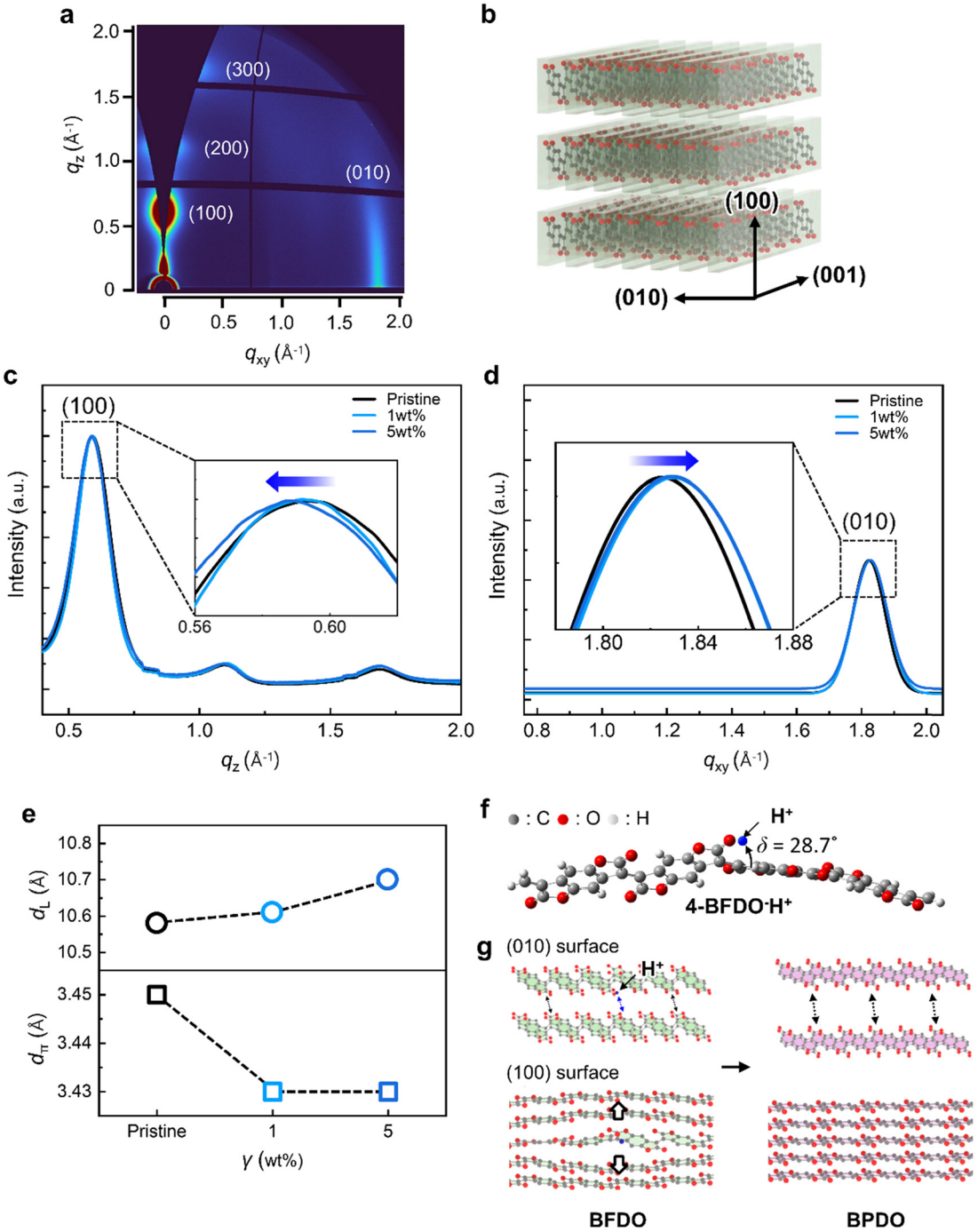

Fig. 2 (a) GIWAXS image of the pristine PBFDO film. (b) Lamellar crystalline structure of PBFDO with the corresponding lattice direction. Extracted GIWAXS spectra along with (c) out-of-plane and (d) in-plane directions. The insets are magnifications of (100) and (010) peaks, respectively. (e) The lamellar d spacing (d_L) and the π–π distance (d_π) of PBFDO/BPDO films with respect to γ. (f) DFT-calculated dihedral angle (δ) between BFDO repeat units in 4-BFDO$^-$H$^+$. (g) Scheme of the changes in the crystalline structure upon BFDO-to-BPDO isomerization.

diminishes.[48] However, the counter ion in the doped PBFDO system is the proton, which is extremely small. Moreover, according to DFT simulations of the 4-BFDO oligomer and proton system, the protons are embedded in the PBFDO backbone, causing distortion of the backbone (Fig. 2f). The DFT simulation results implied that the lack of side chains and the small size of the proton led to little steric hindrance between the PBFDO chain and the proton, resulting in tight binding of the proton to the core of the PBFDO backbone. On the other hand, the oxygens in PBFDO had partially negative charges, resulting in electrostatic repulsion between PBFDO lamellae due to their positions distal from the center of the polymer backbone, oriented toward the periphery. In a doped PBFDO chain, protons are attracted to the negative oxygens on the

periphery of the polymer backbone, reducing this electrostatic repulsion. However, removal of a portion of the protons during hydrothermal treatment would increase the electrostatic repulsion, possibly leading to a greater lamellar spacing (Fig. 2g).

The hydrothermal treatment removed protons from the PBFDO system, while also inducing isomerization from BFDO to BPDO in the chain segments. The π–π interactions in the (010) direction would not be significantly affected by electrostatic interactions between PBFDO chains because both the center and periphery of the polymer backbone participate in these interactions. A proton interacting with a negative polaron in the 4-BFDO oligomer distorted the backbone structure,[49] according to DFT simulations. The removal of protons and the transition from BFDO to BPDO upon hydrothermal treatment

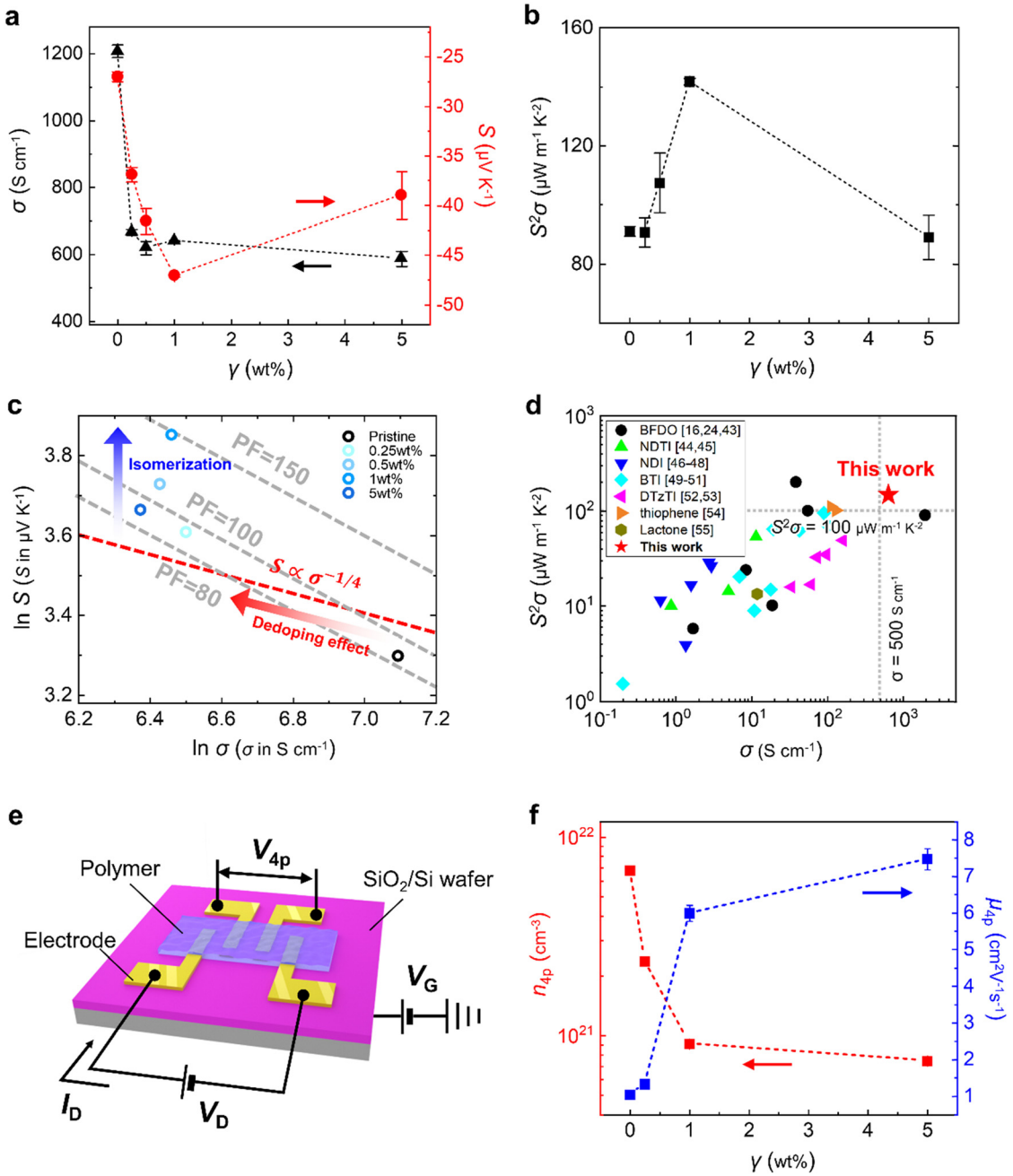

Fig. 3 (a) The electrical conductivity (σ), the Seebeck coefficient (S), and (b) the power factor ($S^2\sigma$) of PBFDO films with respect to γ. (c) The Seebeck coefficient of PBFDO films with respect to the electrical conductivity. The dashed line indicates the isovalue line in the power factor and the dotted line is the curve that follows $S \propto \sigma^{-1/4}$. (d) The power factors of n-type conjugated polymers reported to date as a function of the electrical conductivity, with classification by the backbone moiety (ref. 16, 24 and 43–55). Dotted lines indicate a power factor of 100 μW m^{-1} K^{-2} and an electrical conductivity of 500 S cm^{-1}, respectively. (e) Schematic description of the setup for the measurement of the 4-point-probe field-effect mobility (μ_{4p}). (f) The carrier concentration (n_{4p}) and μ_{4p} of PBFDO films with respect to γ.

are expected to improve the backbone planarity, resulting in a reduction of the π–π distance (Fig. 2f and g).

2.3. Thermoelectric properties of PBFDO/BPDO films

Next, the TE properties of the PBFDO and PBFDO/BPDO films were characterized at different γ values. The pristine PBFDO film showed an electrical conductivity of 1200 S cm^{-1} and a Seebeck coefficient of −27 μV K^{-1}, in good agreement with the values reported in the pioneering work by Tang *et al.* (Fig. 3a).[29] Hydrothermal treatment dramatically decreased the electrical conductivity of the PBFDO film, with the value dropping to below 700 S cm^{-1} even at the small γ of 0.25 wt%. However, increasing γ from 0.25 to 10 wt% caused only marginal decreases in the electrical conductivity from 666 to 575 S cm^{-1}. In contrast, the Seebeck coefficient consistently improved to −47 μV K^{-1} when γ was increased from 0 to 1 wt%. Increasing γ further to 5 wt% caused the Seebeck coefficient to decline to near −40 μV K^{-1}, a value that did not change significantly at higher γ. Both the electrical conductivities and the Seebeck coefficients of PBFDO/BPDO film were maintained for 100 hours under ambient conditions, with less than 10% degradation (Fig. S7, ESI†). The resulting TE power factor ($S^2\sigma$) at γ = 1 wt% was 142 μW m^{-1} K^{-2}, which was 56% higher than that of the pristine PBFDO film (Fig. 3b). Thus, despite a significant reduction in the electrical conductivity, the increase in the Seebeck coefficient led to an exceptionally high power factor.

The above results show that the electrical conductivity dropped markedly upon hydrothermal treatment at γ = 0.25 wt% but did not change substantially with γ, whereas the Seebeck coefficient varied noticeably over the range of γ values studied. The hydrothermal treatment with γ = 0.25 wt% evoked marked changes in both the electrical conductivity and Seebeck coefficient compared to those of the pristine PBFDO film. However, these changes did not significantly affect the power factor because the changes in electrical conductivity (σ) and Seebeck coefficient (S) followed the relation $S \propto \sigma^{-1/4}$ (Fig. 3c). This trade-off relation between σ and S is considered to originate from changes in the carrier concentration, which have opposing effects on the electrical conductivity and Seebeck coefficient.[50] However, increasing γ from 0.25 to 1 wt% dramatically increased the power factor, primarily due to an increase in the Seebeck coefficient, which was significantly higher than expected from the conventional inverse relation $S \propto \sigma^{-1/4}$. In experiments using a lower temperature (80 °C) or shorter treatment time (6 h), conditions under which less isomerization would occur, the electrical conductivity was observed to decrease the values similar to those obtained with hydrothermal treatment at 120 °C and 12 h (Fig. S8, ESI†). These findings indicate that the observed decrease in carrier concentration originated from polaron annihilation by heat and water molecules, rather than from the transition from BFDO to BPDO. Thus, the results indicate that hydrothermal treatment had a dedoping effect, whereas the transition from BFDO to BPDO altered the charge transport characteristics, improving TE performance at the optimized conditions. It is noteworthy that the PBFDO/BPDO film achieved both a high power factor (>100 μW m^{-1} K^{-2}) and high electrical conductivity (>500 S cm^{-1}). Although power factors exceeding 100 μW m^{-1} K^{-2} have recently been reported for a few n-type conjugated polymers, these materials typically exhibit relatively low electrical conductivities[21,29,51–63] and hence are prone to parasitic Joule heating, limiting their practical applications (Fig. 3d). In contrast, PBFDO/BPDO is the first reported n-type conjugated polymer to have a high power factor (>100 μW m^{-1} K^{-2}) combined with a high electrical conductivity (>500 S cm^{-1}).

To further investigate TE charge transport in the PBFDO/BPDO films, the field-effect mobilities were measured using the 4-point-probe method. This method, which is frequently adopted for conductivity measurements, has been applied to the measurement of field-effect mobility, demonstrating effective suppression of errors driven by the contact resistance and the channel shunting effect, both of which can cause considerable errors in organic-based thin films.[64] For the 4-point-probe field-effect mobility (μ_{4p}) measurements, four electrodes were deposited on SiO_2/Si wafer at even intervals prior to deposition of the PBFDO or PBFDO/BPDO film (Fig. 3e). The pristine PBFDO film exhibited a μ_{4p} of 1 cm^2 V^{-1} s^{-1}, which agrees well with the Hall mobility value reported for the PBFDO film (Fig. 3f).[29] This result suggests that the 4-point-probe method successfully captured the bulk carrier mobility, implying that the suppression of the contact resistance and inherently high bulk carrier concentration in the PBFDO film outweighed the accumulation of interfacial charge carriers under the applied gate voltage during the measurement of μ_{4p}. The value of μ_{4p} increased with increasing γ, indicating that the improved chain planarity and crystalline packing induced by hydrothermal treatment promoted charge transport.[65,66]

The carrier concentrations (n_{4p}) of the PBFDO and PBFDO/BPDO films were then calculated from the electrical conductivity and μ_{4p}; using the formula $n_{4p} = \sigma/(e\mu_{4p})$, where e is the electron charge (1.6×10^{-19} C). In contrast to the trend in μ_{4p}, n_{4p} decreased with increasing γ. The decrease in n_{4p} observed on increasing γ from 0.25 to 1 wt% is in accordance with the observed increase in the Seebeck coefficient. Upon further increase of γ from 1 to 5 wt%, however, n_{4p} continued to decrease but the Seebeck coefficient also decreased. This result suggests that an additional factor influenced the Seebeck coefficient at γ = 1 wt%. In conjunction with the exceptionally high values of μ_{4p} at γ = 1 and 5 wt%, a transition in the charge transport would play a primary role in improving the TE performance of the PBFDO/BPDO films, apart from the dedoping effect.

2.4. Charge transport behaviors in PBFDO/BPDO films

To investigate the charge transport mechanisms in the PBFDO and PBFDO/BPDO films, the electrical conductivities of the films were measured over a temperature (T) range of 310 to 88 K (Fig. 4a). The electrical conductivities of numerous conjugated polymers with a wide range of carrier concentrations are well described by the variable-range hopping (VRH) transport model, $\sigma \propto \exp(1/T^a)$, where the exponent a varies between 0.25 and 0.5 depending on the degree of energetic disorder and charge localization length.[67–69] However, the electrical conductivity of the pristine PBFDO film did not conform to the VRH

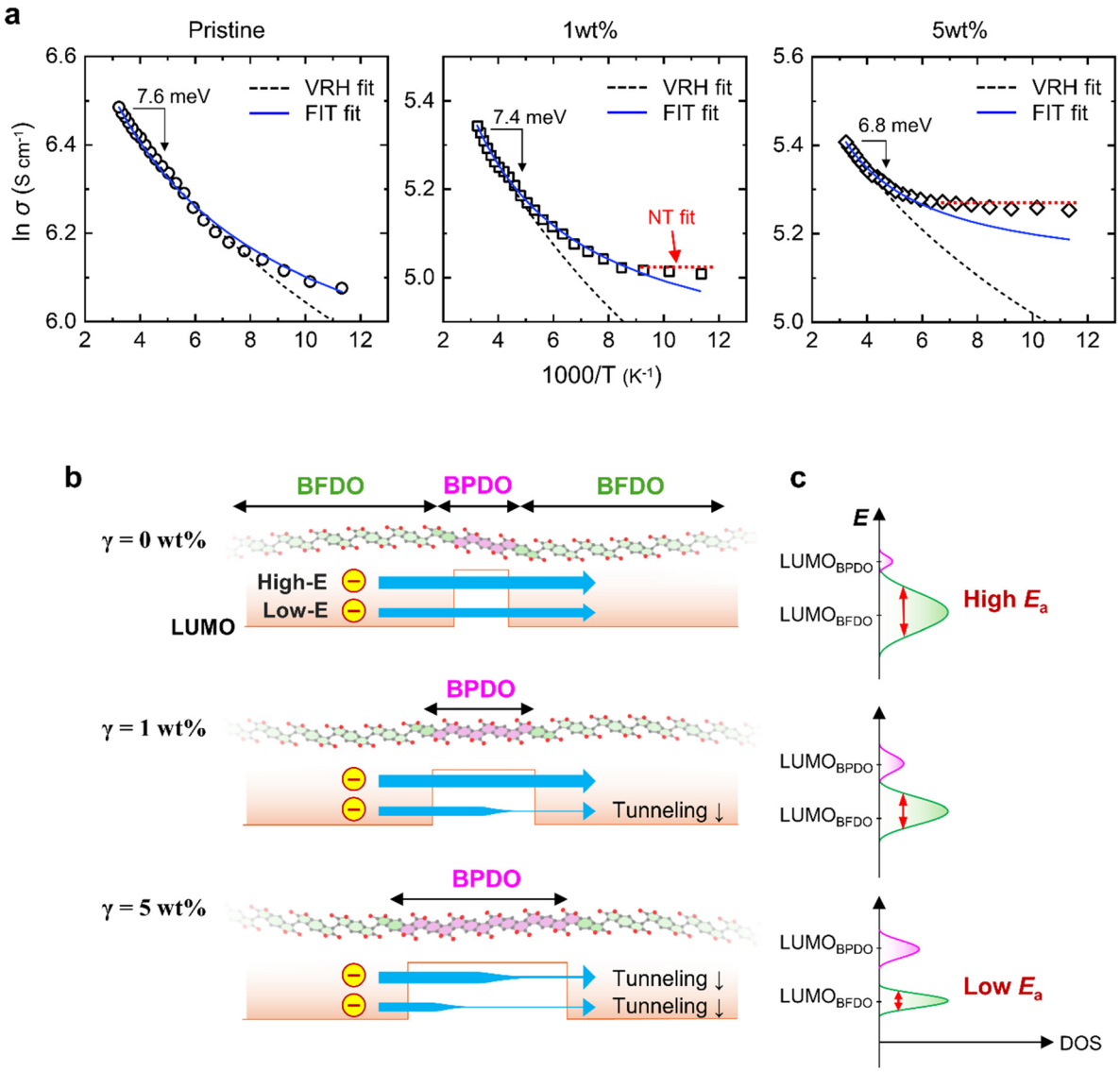

Fig. 4 (a) The electrical conductivity of PBFDO films of varying γ as a function of 1000/T. The dashed, solid, and dotted lines are variable-range hopping (VRH), fluctuation-induced tunneling (FIT), and nuclear tunneling (NT) fit, respectively. (b) Scheme of the charge transport along with the PBFDO chain with respect to γ and (c) corresponding density of states (DOS) distribution near the LUMO level.

model, especially in the low temperature region. Instead, the fluctuation-induced tunneling (FIT) model, $\sigma \propto \exp(T_1/(T - T_0))$ where T_0 and T_1 are constants, successfully described the pristine PBFDO film over the entire temperature range. The FIT model assumes a thin quantum barrier of finite height in the transport pathway, where charge carriers tunnel through the barrier with the help of thermally induced fluctuations.[70,71] The observation that the pristine PBFDO film conforms to the FIT rather than the VRH model is consistent with this film containing a very small amount of BPDO segments, which would be expected to act as a thin quantum barrier in charge conduction as the LUMO level of BPDO is higher than that of BFDO.[30] Thus, the observation of FIT transport in the pristine PBFDO is well aligned with the NMR result, indicating the existence of BPDO segments in the pristine PBFDO.

Similar to the pristine PBFDO film, the hydrothermally treated films were effectively described by the FIT, rather than the VRH model. One difference between the pristine and hydrothermally treated films was that the σ of the treated films was independent of temperature in the low temperature region ($<$150 K). Given that hydrothermal treatment induced minimal morphological changes (Fig. S9, ESI†), the difference in charge transport can be attributed primarily to the BFDO-to-BPDO transition. Additionally, electrons have very small kinetic energies at low temperature; hence, the observation of temperature-independent conductivity at low temperature indicated that the hopping transport was governed by nuclear tunneling (NT), not by thermal activation.[72] These results imply that thermal fluctuations did not significantly affect charge transport in the hydrothermally-treated PBFDO films, in which the higher number of BPDO segments would lead to wider quantum barriers. This notion was supported by the finding that the temperature range over which the conductivity was independent of the

temperature increased as γ increased from 1 to 5 wt%. The difference in transport mode at low temperature between the pristine and hydrothermally treated PBFDO films would be closely related to the changes in Seebeck coefficient upon hydrothermal treatment.

The behavior at low temperatures reflects the transport of charge carriers at relatively low energy, and intrachain rather than interchain transport because of suppressed phonon activation. Therefore, the NT-dominant transport observed in the low temperature region implied that low-energy charge carriers cannot pass through the quantum barrier generated by BPDO segments, neither *via* VRH nor FIT. Low-energy charge carriers would be transported *via* NT driven by the ground-state oscillation, whereas high-energy charge carriers can readily pass through the BPDO segments *via* FIT (Fig. 4b). This difference in transport mode depending on the charge carrier energy would enlarge the mobility gap between high-energy and low-energy polarons. Whereas, high-energy polarons can migrate through both intrachain and interchain transport, low-energy polarons migrate primarily *via* interchain transport due to the low probability of NT. This energy-discriminative charge transport would increase the transport energy level and hence the Seebeck coefficient, in a manner similar to the energy-filtering effect. At γ = 1 wt%, the water content at which the Seebeck coefficient was maximized, the energy-filtering effect by the BPDO segments would be the largest. Increasing γ further to 5 wt% likely caused a significant isomerization from BFDO to BPDO, forming a wider quantum barrier that impeded both low-energy and high-energy charge carrier transport.

Meanwhile, temperature-independent finite conductivity not only occurred over a wider temperature range but also exhibited a higher conductivity value as γ was increased from 1 to 5 wt%. This increase in the finite conductivity at low temperatures can be attributed to a reduction in the activation energy for charge transport. The activation energy (E_a) for charge transport near room temperature was extracted from the slope of the Arrhenius plot of conductivities in the relatively high-temperature region ($1000/T < 4$), using the relation $\sigma \propto \exp(E_a/kT)$, where k is the Boltzmann constant. When γ increased from 0 to 5 wt%, the activation energy decreased from 7.6 to 6.8 meV, implying that overall charge transport was enhanced despite the quantum barriers built by BPDO segments. The changes in activation energy also corresponded to the changes in carrier mobility. A decrease in the activation energy indicated a reduction of energetic disorder,[73] which can be ascribed to improved chain planarity and a densely packed crystalline structure.

On the basis of the above results, we propose the following scenario for the shifts in charge transport behavior caused by hydrothermal treatment. In the pristine PBFDO film, the number of BPDO segments was limited. Hence, charge carriers moving along with chain backbones can readily pass through BPDO segments *via* FIT regardless of their energy. However, the distortion of the chain backbone and the π–π stacking distance resulted in considerable energetic disorder that widened the density of states (DOS) distribution, reducing the overall carrier mobility (Fig. 4c). At γ = 1 wt%, the increased number of BPDO segments led to a wider quantum barrier, which also widened the gap between the mobilities of low-energy and high-energy charge carriers. Meanwhile, the improved chain planarity and crystalline ordering at γ = 1 wt%, reduced the energetic disorder and increased the overall carrier mobility, thereby improving intrachain transport along BFDO segments and interchain transport. Increasing γ to 5 wt% resulted in a very wide intrachain quantum barrier, which impeded FIT of both low-energy and high-energy charge carriers, reducing the energy-filtering effect. In contrast, the further reduction of energetic disorder at γ = 5 wt% would improve both the intrachain transport along BFDO segments and interchain transport, thereby compensating for the wider intrachain quantum barriers for charge transport and increasing the overall carrier mobility.

3. Conclusions

High-performance n-type TE materials based on a conjugated polymer were developed by optimizing TE charge transport through chemical isomerization. Partial isomerization from BFDO to BPDO was observed in PBFDO upon hydrothermal treatment. This partial isomerization had a dedoping effect that reduced the carrier density of the PBFDO film. The hydrothermal treatment-induced increase in the number of BPDO segments, which have a ladder-type structure, greatly improved the chain planarity, which in turn promoted densely-packed crystalline ordering. Such microstructural changes helped to maintain the electrical conductivity, compensating for the dedoping effect of adding increasing amounts of water during hydrothermal treatment. The increase in BPDO content induced by hydrothermal treatment also transformed the charge transport mode. While the pristine PBFDO film was well described by the FIT model, NT-dominant transport behavior was observed at low temperatures after hydrothermal treatment. At an optimal γ value, high-energy charge carriers passed through the quantum barriers generated by BPDO segments *via* FIT, whereas only NT was possible for low-energy charge carriers. This energy-filtering effect increased the Seebeck coefficient by 78% compared to the pristine PBFDO film. As a result, a high power factor of 142 μW m^{-1} K^{-2} was obtained while simultaneously achieving a high electrical conductivity of 640 S cm^{-1}. Thus, through the engineered manipulation of charge transport as well as a high degree of doping, we managed for the first time to develop an n-type conjugated polymer with both high TE power output and low internal resistance.

4. Experimental section

4.1. Materials

Poly[benzodifurandione] (PBFDO) was purchased from Derthon. PBFDO was used as purchased without further purification. PBFDO was stored in a N_2-filled glove box (<2 ppm H_2O, O_2).

4.2. Sample preparation

Pristine PBFDO and PBFDO/BPDO films were prepared on glass substrates for UV-Vis-NIR spectroscopy, Raman spectroscopy and TE characterization on Si/SiO_2 (3000 Å) wafers and Si wafers with native oxide layers for GIWAXS, temperature-dependent electrical conductivity and 4-probe FET measurements. The substrates were rinsed in sequential sonication steps in DI water, acetone, and isopropanol for 15 min each. Both glass substrates and Si wafers were treated with UV/ozone for 20 min to increase surface wettability and to remove residues.

To prepare pristine PBFDO films, a PBFDO solution was spin-coated on the substrate at 3000 rpm for 50 s. The spin-coated films were thermally annealed in N_2 at 100 °C for 10 min and then slowly cooled to 40 °C.

To prepare PBFDO/BPDO films, DI water was added to the PBFDO solution at a specific weight ratio. The mixed solutions were stirred at 120 °C for 12 h to form a PBFDO/BPDO mixture. The PBFDO/BPDO solution was subsequently spin-coated on the substrate at 3000 rpm for 50 s without further purification. The spin-coated films were thermally annealed in N_2 at 100 °C for 10 min and then slowly cooled to 40 °C.

To fabricate samples for TE characterization, temperature-dependent electrical conductivity and 4-probe FET measurements, Au contact electrodes (50 nm) were deposited by thermal evaporation under high vacuum ($<10^{-6}$ Torr).

For NMR analysis, the solvents from pristine PBFDO and hydrothermally treated PBFDO/BPDO solutions were removed under vacuum for more than 24 h. The resulting polymers were dissolved in DMSO-d_6 (7 mg mL^{-1} for PBFDO and PBFDO/BPDO).

Spectroscopic characterization

^{1}H NMR spectra were recorded using a Bruker Avance 400 (400 MHz) in DMSO-d_6. Chemical shifts (δ) are reported in ppm and referenced to the residual proton peak of DMSO-d_6 at δ = 2.50 ppm. PBFDO and PBFDO/BPDO were characterized using a UV-Vis-NIR instrument (V-770, JASCO), a Raman spectrometer (Alpha300R, WITec) equipped with a 532 nm wavelength laser, and an FT-IR spectrometer (Bruker VERTEX 70). The GIWAXS experiment was performed to analyze the crystalline structure of PBFDO and PBFDO/BPDO films using a synchrotron source at 3C and 9A beamlines, and XPS spectra were obtained using the synchrotron source at the 4D beamline of the Pohang Accelerator Laboratory in Korea.

Thermoelectric characterization

Electrical conductivity (σ) was calculated from sheet resistance measured with a four-point probe and the film thickness was measured using an AFM (NanoScope V MultiMode 8, Bruker) (Fig. S10, ESI†). The Seebeck coefficient was obtained using a laboratory-made setup, in which a temperature gradient was applied *via* two Peltier modules. Temperature differences were recorded using T-type thermocouples (copper/constantan) connected to a data acquisition unit (Keysight 34970A), and the generated thermovoltage was measured simultaneously with a nanovoltmeter (Keysight 34420A). Carrier density and carrier mobility were measured using a four-point-probe FET measurement (Keithley 4200 and 2636A).

DFT calculations

The ^{1}H NMR spectra of 4-BFDO and 4-BPDO were recorded and the dihedral angles of 4-BFDO-H^+ were calculated using the Gaussian 09 package. The level of theory was the B3LYP functional with 6-311G+ basis sets.

Author contributions

H. J. performed the data curation, investigation, methodology, validation, and visualization and supported the writing of the draft and conceptualization. J. L. contributed equally to the data curation, investigation, and validation. H. L. provided support for the investigation and visualization. D. K. was primarily responsible for conceptualization, methodology, software development, and validation, and took the lead in writing and revising. K. C. contributed to project supervision, funding acquisition, resource provision, project administration, and review and editing.

Conflicts of interest

There are no conflicts to declare.

Data availability

The raw data supporting the findings of this study are available from the corresponding author upon request.

Acknowledgements

This work was supported by the National Research Foundation of Korea (NRF) grant funded by the Korean government (MSIT) (RS-2025-25413074, RS-2025-00516030 and RS-2023-00234757). The authors thank the Pohang Accelerator Laboratory for providing the synchrotron radiation source at 3C, 9A, and 4D beamlines used in this study.

Notes and references

1 J. He and T. M. Tritt, *Science*, 2017, **357**, eaak9997.
2 Q. Zhang, Y. Sun, W. Xu and D. Zhu, *Adv. Mater.*, 2014, **26**, 6829.
3 O. Bubnova and X. Crispin, *Energy Environ. Sci.*, 2012, **5**, 9345.
4 F. Yao, W. Xie, X. Zhao and H. Gu, *Adv. Compos. Hybrid Mater.*, 2025, **8**, 120.
5 C. Chen, Z. Liu, L. Guo, B. Huo, Q. Sun, L. Liang, C. Du and G. Chen, *Adv. Funct. Mater.*, 2024, **34**, 2411490.
6 T. Zou, D. Zhang, K. Shen, Z. Huang, T. Xu, X. Peng, H. Zhang, Y. Du and L. Sun, *Adv. Compos. Hybrid Mater.*, 2023, **6**, 200.

7 Z. Yu, Y. Wan, M. Zhou, M. H. Mia, S. Huo, L. Huang, J. Xu, Q. Jiang, Z. Zheng, X. Hu and H. He, *Nano-Micro Lett.*, 2025, **17**, 214.
8 Q. Sun, C. Du and G. Chen, *Prog. Mater. Sci.*, 2025, **149**, 101402.
9 M. Dargusch, W. D. Liu and Z. G. Chen, *Adv. Sci.*, 2020, **7**, 2001362.
10 H. Tanaka, K. Kanahashi, N. Takekoshi, H. Mada, H. Ito, Y. Shimoi, H. Ohta and T. Takenobu, *Sci. Adv.*, 2020, **6**, eaay8065.
11 O. Bubnova, Z. U. Khan, A. Malti, S. Braun, M. Fahlman, M. Berggren and X. Crispin, *Nat. Mater.*, 2011, **10**, 429.
12 G. H. Kim, L. Shao, K. Zhang and K. P. Pipe, *Nat. Mater.*, 2013, **12**, 719.
13 J. Ding, Z. Liu, W. Zhao, W. Jin, L. Xiang, Z. Wang, Y. Zeng, Y. Zou, F. Zhang, Y. Yi, Y. Diao, C. R. McNeill, C. A. Di, D. Zhang and D. Zhu, *Angew. Chem., Int. Ed.*, 2019, **58**, 18994.
14 D. Wang, J. Ding, X. Dai, L. Xiang, D. Ye, Z. He, F. Zhang, S. H. Jung, J. K. Lee, C. A. Di and D. Zhu, *Adv. Mater.*, 2023, **35**, 2208215.
15 D. Yuan, W. Liu and X. Zhu, *Chem. Soc. Rev.*, 2023, **52**, 3842.
16 H. T. Nicolai, M. Kuik, G. A. H. Wetzelaer, B. De Boer, C. Campbell, C. Risko, J. L. Brédas and P. W. M. Blom, *Nat. Mater.*, 2012, **11**, 882.
17 G. Zuo, M. Linares, T. Upreti and M. Kemerink, *Nat. Mater.*, 2019, **18**, 588.
18 J. Liu, G. Ye, B. V. D. Zee, J. Dong, X. Qiu, Y. Liu, G. Portale, R. C. Chiechi and L. J. A. Koster, *Adv. Mater.*, 2018, **30**, 1804290.
19 Y. Xia, K. Sun and J. Ouyang, *Adv. Mater.*, 2012, **24**, 2436.
20 Y. Wang, C. Zhu, R. Pfattner, H. Yan, L. Jin, S. Chen, F. Molina-Lopez, F. Lissel, J. Liu, N. I. Rabiah, Z. Chen, J. W. Chung, C. Linder, M. F. Toney, B. Murmann and Z. Bao, *Sci. Adv.*, 2017, **3**, e1602076.
21 Z.-D. Yu, Y. Lu, Z.-Y. Wang, H.-I. Un, S. J. Zelewski, Y. Cui, H.-Y. You, Y. Liu, K.-F. Xie, Z.-F. Yao, Y.-C. He, J.-Y. Wang, W.-B. Hu, H. Sirringhaus and J. Pei, *Sci. Adv.*, 2023, **9**, eadf3495.
22 Y. Kuang, M. Yang, L. Pan, G. Ye, S. Shao, C. Duan and J. Liu, *Chem. Mater.*, 2024, **36**, 11075.
23 S. Gámez-Valenzuela, J. Li, S. Ma, S. Y. Jeong, H. Y. Woo, K. Feng and X. Guo, *Angew. Chem., Int. Ed.*, 2024, **63**, e202408537.
24 C.-Y. Yang, Y.-F. Ding, D. Huang, J. Wang, Z.-F. Yao, C.-X. Huang, Y. Lu, H.-I. Un, F.-D. Zhuang, J.-H. Dou, C.-A. Di, D. Zhu, J.-Y. Wang, T. Lei and J. Pei, *Nat. Commun.*, 2020, **11**, 3292.
25 G. Ma, M. Leng, S. Li, Z. Cao, Y. Cao, D. P. Tabor, L. Fang and X. Gu, *J. Mater. Chem. C*, 2022, **10**, 13896.
26 S. Wang, H. Sun, U. Ail, M. Vagin, P. O. Å. Persson, J. W. Andreasen, W. Thiel, M. Berggren, X. Crispin, D. Fazzi and S. Fabiano, *Adv. Mater.*, 2016, **28**, 10764.
27 P. Wei, J. H. Oh, G. Dong and Z. Bao, *J. Am. Chem. Soc.*, 2010, **132**, 8852.
28 P. Rossi, F. Pallini, G. Coco, S. Mattiello, W. L. Tan, L. Mezzomo, M. Cassinelli, G. Lanzani, C. R. McNeill, L. Beverina and M. Caironi, *Adv. Mater. Interfaces*, 2023, **10**, 2202416.
29 H. Tang, Y. Liang, C. Liu, Z. Hu, Y. Deng, H. Guo, Z. Yu, A. Song, H. Zhao, D. Zhao, Y. Zhang, X. Guo, J. Pei, Y. Ma, Y. Cao and F. Huang, *Nature*, 2022, **611**, 271.
30 Z. Ke, A. Abtahi, J. Hwang, K. Chen, J. Chaudhary, I. Song, K. Perera, L. You, K. N. Baustert, K. R. Graham and J. Mei, *J. Am. Chem. Soc.*, 2023, **145**, 3706.
31 J. Hwang, Q. Zhao, M. Ahmed, A. C. Yakisan, M. F. Espenship, J. Laskin, B. M. Savoie and J. Mei, *Angew. Chem., Int. Ed.*, 2024, **63**, e202401465.
32 P. Sun, B. Wei, J. Zhang, J. M. Tomczak, A. M. Strydom, M. Søndergaard, B. B. Iversen and F. Steglich, *Nat. Commun.*, 2015, **6**, 7475.
33 G. J. Snyder and E. S. Toberer, *Nat. Mater.*, 2008, **7**, 105.
34 I. Zozoulenko, A. Singh, S. K. Singh, V. Gueskine, X. Crispin and M. Berggren, *ACS Appl. Polym. Mater.*, 2019, **1**, 83.
35 J. Kim, D. Ju, S. Kim and K. Cho, *Adv. Funct. Mater.*, 2024, **34**, 2309156.
36 D. Herrmann, S. Niesar, C. Scharsich, A. Köhler, M. Stutzmann and E. Riedle, *J. Am. Chem. Soc.*, 2011, **133**, 18220.
37 D. Ju, D. Kim, H. Yook, J. W. Han and K. Cho, *Adv. Funct. Mater.*, 2019, **29**, 1905590.
38 D. Ohayon, G. Quek, B. R. P. Yip, F. Lopez-Garcia, P. R. Ng, R. J. Vázquez, D. V. Andreeva, X. Wang and G. C. Bazan, *Adv. Mater.*, 2024, **36**, 2410512.
39 S. Garreau, G. Louarn, J. P. Buisson, G. Froyer and S. Lefrant, *Macromolecules*, 1999, **32**, 6807.
40 J. Ouyang, C. W. Chu, F. C. Chen, Q. Xu and Y. Yang, *Adv. Funct. Mater.*, 2005, **15**, 203.
41 D. Ju, J. Kim, H. Yook, J. W. Han and K. Cho, *Nano Energy*, 2021, **90**, 106604.
42 M. D. Peeks, C. E. Tait, P. Neuhaus, G. M. Fischer, M. Hoffmann, R. Haver, A. Cnossen, J. R. Harmer, C. R. Timmel and H. L. Anderson, *J. Am. Chem. Soc.*, 2017, **139**, 10461.
43 W. Zhu, X. Qiu, J. E. M. Laulainen, H. L. Un, X. Ren, M. Xiao, G. Freychet, P. Vacek, D. Tjhe, Q. He, W. Wood, Z. Wang, Y. Zhang, Z. Qu, J. Asatryan, J. Martin, M. Heeney, C. R. McNeill, P. A. Midgley, I. E. Jacobs and H. Sirringhaus, *Adv. Mater.*, 2024, **36**, 2310480.
44 L. Deng and G. Chen, *Nano Energy*, 2021, **80**, 105448.
45 E. Lim, K. A. Peterson, G. M. Su and M. L. Chabinyc, *Chem. Mater.*, 2018, **30**, 998.
46 M. L. Chabinyc, M. F. Toney, R. J. Kline, I. McCulloch and M. Heeney, *J. Am. Chem. Soc.*, 2007, **129**, 3226.
47 T. Kurosawa, Y. Yamashita, Y. Kobayashi, C. P. Yu, S. Kumagai, T. Mikie, I. Osaka, S. Watanabe, J. Takeya and T. Okamoto, *Macromolecules*, 2024, **57**, 328.
48 M. Xiong, X.-Y. Deng, S.-Y. Tian, K.-K. Liu, Y.-H. Fang, J.-R. Wang, Y. Wang, G. Liu, J. Chen, D. R. Villalva, D. Baran, X. Gu and T. Lei, *Nat. Commun.*, 2024, **15**, 4972.
49 Z. Ke, J. Chaudhary, L. Q. Flagg, K. N. Baustert, A. O. Yusuf, G. Liu, L. You, K. R. Graham, D. M. DeLongchamp and J. Mei, *Adv. Funct. Mater.*, 2024, **34**, 2400255.

50 A. M. Glaudell, J. E. Cochran, S. N. Patel and M. L. Chabinyc, *Adv. Energy Mater.*, 2015, **5**, 1401072.
51 Z. D. Yu, Y. Lu, Z. F. Yao, H. T. Wu, Z. Y. Wang, C. K. Pan, J. Y. Wang and J. Pei, *Angew. Chem., Int. Ed.*, 2024, **63**, e202405139.
52 Y. Wang and K. Takimiya, *Adv. Mater.*, 2020, **32**, e2002060.
53 Y. Wang, M. Nakano, T. Michinobu, Y. Kiyota, T. Mori and K. Takimiya, *Macromolecules*, 2017, **50**, 857.
54 J. Han, Y. Jiang, E. Tiernan, C. Ganley, Y. Song, T. Lee, A. Chiu, P. McGuiggan, N. Adams, P. Clancy, T. P. Russell, P. E. Hopkins, S. M. Thon, J. D. Tovar and H. E. Katz, *Angew. Chem., Int. Ed.*, 2023, **62**, 202219313.
55 J. Liu, G. Ye, H. G. O. Potgieser, M. Koopmans, S. Sami, M. I. Nugraha, D. R. Villalva, H. Sun, J. Dong, X. Yang, X. Qiu, C. Yao, G. Portale, S. Fabiano, T. D. Anthopoulos, D. Baran, R. W. A. Havenith, R. C. Chiechi and L. J. A. Koster, *Adv. Mater.*, 2021, **33**, e2006694.
56 X. Peng, G. Ye, L. Zhang, Y. Kuang, S. Shao and J. Liu, *Macromolecules*, 2024, **57**, 7156.
57 K. Feng, J. Wang, S. Y. Jeong, W. Yang, J. Li, H. Y. Woo and X. Guo, *Adv. Sci.*, 2023, **10**, e2302629.
58 J. Li, M. Liu, K. Yang, Y. Wang, J. Wang, Z. Chen, K. Feng, D. Wang, J. Zhang, Y. Li, H. Guo, Z. Wei and X. Guo, *Adv. Funct. Mater.*, 2023, **33**, 2213911.
59 W. Yang, K. Feng, S. Ma, B. Liu, Y. Wang, R. Ding, S. Y. Jeong, H. Y. Woo, P. K. L. Chan and X. Guo, *Adv. Mater.*, 2024, **36**, 2305416.
60 Y. Shi, J. Li, H. Sun, Y. Li, Y. Wang, Z. Wu, S. Y. Jeong, H. Y. Woo, S. Fabiano and X. Guo, *Angew. Chem., Int. Ed.*, 2022, **61**, 202214192.
61 Y. Li, W. Wu, Y. Wang, E. Huang, S. Y. Jeong, H. Y. Woo, X. Guo and K. Feng, *Angew. Chem., Int. Ed.*, 2024, **63**, e202316214.
62 S. Deng, Y. Kuang, L. Liu, X. Liu, J. Liu, J. Li, B. Meng, C. A. Di, J. Hu and J. Liu, *Adv. Mater.*, 2024, **36**, 2309679.
63 M. Alsufyani, M. A. Stoeckel, X. Chen, K. Thorley, R. K. Hallani, Y. Puttisong, X. Ji, D. Meli, B. D. Paulsen, J. Strzalka, K. Regeta, C. Combe, H. Chen, J. Tian, J. Rivnay, S. Fabiano and I. McCulloch, *Angew. Chem., Int. Ed.*, 2022, **61**, e202113078.
64 H. H. Choi, Y. I. Rodionov, A. F. Paterson, J. Panidi, D. Saranin, N. Kharlamov, S. I. Didenko, T. D. Anthopoulos, K. Cho and V. Podzorov, *Adv. Funct. Mater.*, 2018, **28**, 1707105.
65 Y. Kim, H. Hwang, N. K. Kim, K. Hwang, J. J. Park, G. I. Shin and D. Y. Kim, *Adv. Mater.*, 2018, **30**, 1706557.
66 D. H. Kim, D. Y. Lee, H. S. Lee, W. H. Lee, Y. H. Kim, J. I. Han and K. Cho, *Adv. Mater.*, 2007, **19**, 678.
67 A. N. Aleshin, J. Y. Lee, S. W. Chu, S. W. Lee, B. Kim, S. J. Ahn and Y. W. Park, *Phys. Rev. B: Condens. Matter Mater. Phys.*, 2004, **69**, 214203.
68 A. Masarrat, A. Bhogra, R. Meena, R. Urkude, A. Niazi and A. Kandasami, *J. Electron. Mater.*, 2022, **51**, 3350.
69 H. Abdalla, G. Zuo and M. Kemerink, *Phys. Rev. B*, 2017, **96**, 241202.
70 T. Stedman, K. Wei, G. S. Nolas and L. M. Woods, *Phys. Chem. Chem. Phys.*, 2015, **17**, 27883.
71 D. Kim, Y. Park, D. Ju, G. Lee, W. Kwon and K. Cho, *Chem. Mater.*, 2021, **33**, 4853.
72 K. Asadi, A. J. Kronemeijer, T. Cramer, L. Jan Anton Koster, P. W. M. Blom and D. M. De Leeuw, *Nat. Commun.*, 2013, **4**, 1710.
73 I. I. Fishchuk, A. Kadashchuk, S. T. Hoffmann, S. Athanasopoulos, J. Genoe, H. Bässler and A. Köhler, *Phys. Rev. B: Condens. Matter Mater. Phys.*, 2013, **88**, 125202.

